MXene nanoflakes decorating ZnO tetrapods for enhanced performance of skin-attachable stretchable enzymatic electrochemical glucose sensor

Valerii Myndrul, Emerson Coy, Nataliya Babayevska, Veronika Zahorodna, Vitalii Balitskyi, Ivan Baginskiy, Oleksiy Gogotsi, Mikhael Bechelany, Maria Teresa Giardi, Igor Iatsunskyi

HAL Id: hal-03671010

https://hal.umontpellier.fr/hal-03671010

Submitted on 15 Nov 2022

MXene Nanoflakes Decorating ZnO Tetrapods for Enhanced Performance of Skin-attachable Stretchable Enzymatic Electrochemical Glucose Sensor

Valerii Myndrul[a*], Emerson Coy[a], Nataliya Babayevska[a], Veronika Zahorodna[c], Vitalii Balitskyi[c], Ivan Baginskiy[c], Oleksiy Gogotsi[c], Mikhael Bechelany[d], Maria Teresa Giardi[e,f] and Igor Iatsunskyi[a*]

[a]NanoBioMedical Centre, Adam Mickiewicz University, 3, Wszechnicy Piastowskiej Str., 61-614 Poznan, Poland, igoyat@amu.edu.pl, valmyn@amu.edu.pl

[b] Materials Research Center, Krzhizhanovskogo street, 3, 03680, Kyiv, Ukraine

[c] Institut Européendes Membranes, IEM, UMR5635, Univ Montpellier, ENSCM, CNRS, 34095 Montpellier CEDEX5, France

[d] Biosensor Srl, Via Degli Olmetti 44, 00060 Formello Rome, Italy

[e] Istituto di Cristallografia, CNR Area Della Ricerca di Roma, 00015 Monterotondo Scalo Rome, Italy

ABSTRACT:

Continuous painless glucose monitoring is the greatest desire of more than 422 million diabetics worldwide. Therefore, new non-invasive and convenient approaches to glucose monitoring are more in demand than other tests microanalytical diagnostic tools. Besides, blood glucose detection can be replaced by continuous glucose monitoring of other human biological fluids (e.g. sweat) collected non-invasively. In this study, a skin-attachable and stretchable electrochemical enzymatic sensor based on ZnO tetrapods (TPs) and a new class of 2D materials - transition metal carbides, known as MXene, was developed and their electroanalytical behavior was tailored for continuous detection glucose in sweat. The high specific area of ZnO TPs and superior electrical conductivity of MXene ($Ti_3C_2T_x$) nanoflakes enabled to produce enzymatic electrochemical glucose biosensor with enhanced sensitivity in sweat sample (29 µA mM^{-1} cm^{-2}), low limit of detection (LOD $\approx$ 17 µM), broad linear detection range (LDR = 0.05 – 0.7 mM) that satisfices glucose detection application in human sweat, and advanced mechanical stability (up to 30% stretching) of the template. The developed skin-attachable stretchable electrochemical electrodes allowed to monitor the level of glucose in sweat while sugar uptake and during physical activity. Continuous in vivo monitoring of glucose in sweat obtained during 60 min correlated well with data collected by a conventional amperometric blood glucometer in vitro mode. Our findings demonstrate the high potential of developed ZnO/MXene skin-attachable stretchable sensors for biomedical applications on a daily basis.

KEYWORDS: MXene; ZnO tetrapods; glucose sensor; glucose oxidase; sweat glucose monitoring.

1. INTRODUCTION

With the increased demand for real-time monitoring of health-related small molecular weight biomarkers, the portable medical device industry has grown rapidly over the past decade (Cucciniello et al., 2021). These devices have an advantage over conventional medical detection tools since they are user-friendly and require non-invasive biological fluids such as sweat, saliva, or tears (Chen et

al., 2017). With remote patient monitoring capabilities and non-invasiveness, portable medical devices are good candidates for painless harvesting of physiologically relevant data in real-time mode. For example, skin-attached, stretchable portable devices can meet the requirements of painless and continuous glucose monitoring in diabetic patients, eliminating the daily inconvenience of finger-prickling. While real-time glucose monitoring can minimize the risk of serious complications caused by diabetes, and also can provide insights into body glucose dynamics, especially after mealtimes, during physical activity and at rest.

Although many approaches to non-invasive glucose monitoring are currently proposed, portable and wearable devices are still poorly implemented on a large industrial scale, despite their grown potential and advantages (Lee et al., 2017). Such a slow implementation is mainly due to the unclear correlation between sweat and blood glucose levels (Lee et al., 2017; Sempionatto et al., 2021). Nevertheless, this drawback does not negate the fact that sweat glucose still can qualitatively indicate hypo- or hyperglycemia and the necessity for self-care intervention to control and stabilize blood glucose levels. Besides, the skin-attachable sweat glucose sensor performance can be improved by developing novel and effective transducers. In this case, significant attention should be given to the materials and composites with enhanced catalytic activity towards glucose oxidation and superior electrical conductivity, particularly in complex matrices, i.e. blood or sweat (Zhou et al., 2019).

Among all known semiconductors, the nanoscale zinc oxide (ZnO) is considered to be one of the most suitable for biomedical applications. A variety of morphologies, the enhanced surface to volume ratio, high isoelectric point (IEP, ~ 9.5), high electron transport capacity, and biocompatibility are just a few of its many superior physical-chemical properties (Myndrul et al., 2020; Pavlenko et al., 2020; Tereshchenko et al., 2016). Today, ZnO still meets scientists' expectations and is increasingly used in a variety of detection techniques, such as optical (Myndrul et al., 2021), electronic (Wang et al., 2019), SPR (Kuranaga et al., 2020), SERS (Y. Zhai et al., 2019), and piezoelectric (bio)sensors (Zhao et al., 2015). Among ZnO nanostructures, ZnO tetrapods (ZnO TPs) occupy an important position on biosensing development because of their higher active surface area provided by the large pods and highly porous 3D interconnected networks, which provide more sites for analyte adsorption and, as a consequence, better sensitivity to small molecular weight compounds detection (Lei et al., 2012a; Mishra and Adelung, 2018a). It was recently reported that the high catalytic activity of ZnO TPs towards the sulfonamide antibacterial degradation, which was 2-3 times higher when compared with ZnO nanoparticles or nanoflowers (Yi et al., 2018). The enhanced surface to volume ratio and high catalytic activity were the reasons for the higher sensitivity of TP ZnO to L-lactic acid than that of ZnO nanorods with similar analytical performance (Lei et al., 2012a; Zhao et al., 2014). However, the high electrical resistivity of ZnO TPs is a significant drawback for electrochemical sensing applications. Yet, there is still a possibility to improve the electrochemical sensor performance by integrating ZnO TPs with high conductive 2D nanomaterials (Theerthagiri et al., 2019).

Although the history of 2D materials is short and has not even crossed the 20-year mark (since the synthesis of graphene in 2004) (Novoselov et al., 2004), have emerged in a wide variety of scientific areas. 2D materials have become popular due to the enhanced optoelectronic properties that differ from those of conventional bulk materials (Kang et al., 2019). Until now, particular attention has been paid to the high catalytic activity of those atomically thin structures driven by enhanced surface area and carrier transport. In this context, 2D materials are used to enhance the water splitting and CO_2 reduction performances (Fan et al., 2021). while high stability and biocompatibility make them attractive for medical and biological applications (Tao et al., 2019). For example, biosensors based on 2D sheets of graphene, MoS_2, and MXene (transition metal carbides, e.g. $Ti_3C_2T_x$) (VahidMohammadi et al., 2021) demonstrate enhanced sensitivity towards proteins, bacteria, H_2O_2, and glucose detection.(Zeng et al., 2021) However, the low electrical conductivity of MoS_2, high hydrophobicity of both graphene and MoS_2, and laborious functionalization can complicate the biosensing performance.(Kalambate et al., 2019) In contrast, MXene has advantages over graphene and MoS_2 since it possesses outstanding metal-like conductivity and hydrophilic surface with termination groups (–OH, =O and –F), facilitating the functionalization process. Composites based

on MXene and ZnO exhibit unique properties that enable application in various applications, including solar cells (Hou and Yu, 2021), water splitting (Sreedhar and Noh, 2021), electromagnetic wave absorption (Qian et al., 2017), photocatalytic performance (Khadidja et al., 2021), light-emitting diodes (Lu et al., 2020), and sensing (Yang et al., 2021). Moreover, due to the enhanced catalytic activity of ZnO/MXene composites (Lv et al., 2021), it may be an ideal candidate for biosensor applications, especially for electrochemical glucose detection.

In this report, catalytically active composites of ZnO TPs/MXene were prepared and deposited on a stretchable electrode as an electroactive transducer layer for the qualitative analysis of glucose in Phosphate-buffered saline (PBS), artificial and human sweat. To the best of our knowledge, this is the first proposed protocol for decorating ZnO nanostructures with MXene nanoflakes and not vice versa. The structural, chemical, electrochemical and optical properties of produced composites were analyzed. ZnO TPs/MXene/GOx nanocomposites exhibited enhanced catalytic activity towards glucose oxidation in PBS and artificial sweat compared to the pristine ZnO TPs and MXene. The higher catalytic activity of ZnO TPs/MXene resulted in a better sensitivity and a lower limit of detection (LOD) for glucose in PBS and artificial sweat. Moreover, the low applied negative potential of -0.24 V allowed to avoid the impact of the interference species that could contribute to the response of ZnO TPs/MXene/GOx-based electrode. The ZnO TPs/MXene stretching experiments have shown the high mechanical stability (up to 30% of strain) of developed electrodes. We also performed in vivo measurements of glucose in sweat, and we demonstrated the good correlation of obtained data with one collected by a conventional amperometric blood glucometer.

2. EXPERIMENTAL SECTION
2.1. Materials.

(3-Aminopropyl)triethoxysilane (APTES, purity ≥98%) glucose oxidase (GOx) (№ G7141), D-(+)-Glucose (№ 8270), Nafion 117 (~5%) containing solution (№ 70160), Glutaraldehyde (GA, 50 wt. % in H_2O), Sodium hydroxide (NaOH, grade ≥98%), Zn powder (№ 324930, purity of 99,9%), ascorbic acid (AA) (№ PHR1008) , urea (purity ≥99%), uric acid (UA, purity ≥99%, crystalline) dopamine (№ H8502), sodium chloride (NaCl , grade ≥99%), potassium chloride (KCl) (№ P3911), glycine (purity ≥99%), Ammonium hydroxide solution (NH_4OH) (№ 221228), were purchased from Sigma Aldrich. PBS, pH 7.4 was used as the diluent for glucose oxidase and glucose dissolution. Polyethylene terephthalate (PET) was provided by Policrom Screens S.P.A. (Carvico, BG, Italy). Silver reference electrodes and contacts on all produced electrodes were printed using LOCTITE® ECI 1010 E&C (Henkel); working and reference electrodes were printed using LOCTITE® EDAG 407C E&C (Henkel). Lithium fluoride (LiF, 98.5% grade) powder and hydrochloric acid (HCl, 37 wt. %) were purchased from Alfa Aesar.

2.2. Instruments.

Morphologies of the ZnO TPs, MXene and ZnO TPs/MXene were investigated by scanning electron microscopy (SEM) (JEOL, JSM7001F) with a dispersive energy X-ray (EDX) analyzer and transmission electron microscopy (TEM) (JEOL ARM 200F) high-resolution transmission electron microscope (200 kV) with an EDX analyzer. The structural state of samples was analyzed by means of X-ray diffraction (XRD) (PANalytical, X'pert3pro MRD diffractometer) working with a Cu lamp (λ = 1.5418 Å). Raman spectrum was measured by means of a Renishaw micro-Raman spectrometer with a confocal microscope. The samples' optical properties (absorbance, photoluminescence) have been studied with Ocean Optics spectrophotometer QE65pro. Electrochemical measurement and glucose detection, including cycling voltammetry and chronoamperometry regimes, were performed using potentiostats ER466 and GAMRY 620. The sonication of the MXene sheets to divide them into MXene nanoflakes was performed by Sonifier ultrasonic processor (SFX 20:0.55).

2.3. Preparation of ZnO TPs.

ZnO tetrapods (ZnO TPs) were obtained by the simple catalyst-free oxidative-metal-vapour-transport method. The method was based on thermal evaporation of Zn powder at 1000°C for 1h in the air in a ceramic crucible (Tawale et al., 2010). After the reaction, the white powder of ZnO was deposited, which confirmed the oxidation of zinc metal powder.

2.4. Preparation of MXene.

$Ti_3C_2T_x$ MXene was prepared by etching Ti_3AlC_2 (MAX-phase) ternary carbide using MILD method in a solution of lithium fluoride (LiF) in hydrochloric (HCl) acid (Alhabeb et al., 2017). Etching mixture was prepared from 40 mL of 12 M HCl (37%), 10 mL of DI-water and then 3.2 g of LiF are dissolved in this solution. The mixture was placed in a plastic container with a volume of 50 mL. Then 2 g of Ti_3AlC_2 powder with particle sizes of less than 40 μm is gradually added into etching solution under continuous stirring for 24 hours at 25ºC. Then MXene slurry was rinsed with DI-water via repetitive centrifugation. As-prepared MXene slurry is further processed to obtain a colloidal solution of separated MXene flakes using mild delamination procedure assisted by intercalation of Li^+ ion between Ti_3C_2 sheets with following the separation of MXene into colloidal solution in water (Alhabeb et al., 2017). We used the following protocol for the delamination: 2 g of lithium chloride (LiCl) were added to 40 mL of DI-water in 50 mL plastic container. Etched MXene slurry is added to the prepared solution. The process is performed at 35 ºC for 24 hours under stirring. After that, MXene slurry is rinsed via repetitive cycles of centrifuging. Purity of MXene is confirmed by XRD analysis. After synthesis MXene sediment is stored at -18°C.

2.5. Fabrication of skin-attachable, stretchable electrodes.

The skin-attachable electrodes made of Silver/Silver-NaCl/Carbon in PTU (125 μm thickness) were produced by a conventional screen printing method, property of Eastprint-USA (http://www.eastprint.com/electrodes-biosensors.html) under design property of Biosensor srl (https://www.biosensor-srl.eu/).

2.6. Preparation of ZnO/MXene based electrode.

The ready-to-use MXene sheets were then placed in a PBS solution and sonicated (for 20 minutes at 70% ultrasonic processor power) to crush into MXene nanoflakes for use in the ZnO TPs decorating process. Once ready, MXene nanoflakes were then mixed with ZnO TPs in proportion 1:2 (1 mg/ml MXene and 2 mg/ml ZnO TPs in DI water) to prepare combined ZnO TPs/MXene structure. The sample was then investigated on SEM in order to confirm the coverage of ZnO TPs by MXene nanoflakes, and the result showed the inhomogeneity of the coverage (SI, Fig. 1S). In order to improve the uniformity, ZnO TPs were treated with 2% ATPES solution (in anhydrous EtOH 99.6%) to achieve functional groups on their surfaces. This process was followed by 3-times rinsing of ZnO TPs (2 times in EtOH and 1 time in PBS) to eliminate APTES remains. The functionalized ZnO TPs were then mixed again with MXene in 1:2 (1 mg/ml MXene and 2 mg/ml ZnO TPs in DI water) to prepare combined ZnO TPs/MXene structure. The process of mixing was performed under sonicating conditions (for 2 hours at RT). After the sonication, the sample was rinsed in DI water and centrifuged 3 times to remove unbound MXene nanoflakes and remove excess water.

The prepared ZnO TPs/MXene sample was mixed with Nafion (1 mL of 2% EtOH solution, neutralized to pH = 7, by use of 0.1 M NaOH). The droplet (8 μL) of this mixture was placed on the working electrode of the stretchable sensor and dried for 1 h at 65 °C. Once cooled, the sensor's working electrode was then cross-linked by GA (30 min, RT) and GOx was added (8μL of 20 mg/mL in PBS, for 12 hours at 4°C) to achieve a selective layer toward glucose. After that, the skin-attachable and stretchable sensor were coated by the additional layer of Nafion polymer (5 μL of 2 % solution in EtOH neutralized to pH = 7) and stored for 1 day at 4°C before use. The sketch diagram (SI, Fig. 2S) depicts MXene nanoflakes and ZnO TPs fabrication stages, the deposition of ZnO TPs/MXene

composite on the skin-attachable, stretchable electrode and selective layer formation using GOx and Nafion.

For the comparative analysis of the electrochemical and structural properties and the glucose detection parameters, three types of electrodes were prepared and titled as ZnO TPs/GOx-based electrode, MXene/GOx-based electrode, and ZnO TPs/MXene/GOx-based electrode. The stability of all prepared electrodes was tested in different pH.

2.7. Electrochemical glucose detection in PBS and artificial sweat.

The fabricated electrodes were initially tested in PBS (pH 7.4) with a change of glucose concentration in the experimental cell. The electrochemical properties of ZnO TPs/GOx-, MXene/GOx-, and ZnO TPs/MXene/GOx-based electrodes were studied using CV measurements at scan rate of 40 mV/s.

Chronoamperometry was performed to determine glucose using ZnO TPs-based electrode with an applied potential of -0.43 V (*vs* Ag), MXene/GOx-based electrode with applied a potential of -0.21 V, and for the ZnO TPs/MXene-based electrode the applied potential was equal to -0.24 V. Chronoamperometry measurements for the ZnO TPs/MXene/GOx-based electrode were carried out in artificial sweat (pH 6.5) at the same applied potential (-0.24 V) as for PBS. Artificial sweat was prepared according to the protocol EN1811:2012 and consisted of NaCl (0.5%), KCl (0.1%), and urea (0.1%), while the pH was adjusted to 6.5 by use of NH_4OH (Meng et al., 2021). The selectivity of ZnO TPS/MXene-based electrode to glucose in artificial sweat was evaluated by means of chronoamperometry with the sequential addition of 0.1 mM AA, 0.5 mM urea, 50 µM UA, 0.05 mM dopamine, 10 mM NaCl, 10 mM KCl, and 0.1 mM glycine.

All experiments were repeated at least three times and all parameters (LODs, sensitivities, electron transfer rates, etc.) were calculated as means±standard error.

2.8. On-body sweat analysis

On-body sweat analysis was performed in a healthy subject aged 30 years. During the real-time glucose monitoring, the electrode was tightly attached to the wet skin, the contacts were connected to the potentiostat, and the data were displayed on a laptop screen. Chronoamperometry measurements were carried out at the same applied potential (-0.24 V) as it for artificial sweat. The volunteer was asked to take sweets and do exercises on a command. Additional invasive glucose measurements (8 discrete points) were done using a commercially available glucometer (VGM01, VivaCheck Ino).

2.9. Electrode stretching tests.

Stretchability was tested using a lab-made device capable of stretching the firmly attached electrode. The discrete values of the applied strain varied from 0 to 35%. The response was measured by potentiostat operating in amperometric mode. The 3-electrode system was sandwiched between slides to ensure a constant analyte value during experiments. Various glucose concentrations (0.1 mM, 0.2 mM, 0.5 mM, 0.7 mM, and 1 mM) were tested on the electrodes with 0%, 15%, and 30% elongation to evaluate the stability of the electrodes under various strains.

3. RESULTS AND DISCUSSION
3.1. Choice of Materials

As mentioned in the "Introduction" section, ZnO is one of the widely used materials in sensor and biosensor technologies, and such popularity is due to its high stability, biocompatibility, and enhanced surface to volume ratio (when considering hierarchical structures). Since the stability of the transducer, as well as its biocompatibility, are the most important parameters during the electrochemical biosensor performance, ZnO was considered the most suitable material to be used in our experiments. ZnO in the shape of tetrapods (ZnO TPs) has the highest active surface when compared with the other ZnO morphologies, and therefore, the use of ZnO TPs can enhance the

efficiency of detection performance (Lei et al., 2012b; Mishra and Adelung, 2018b). The choice of MXene nanoflakes for ZnO decoration was based on the assumption that MXene would facilitate the charge transfer rate between the electrolyte and ZnO, as it was reported for the ZnO nanorods and MXene sheets (Liu and Chen, 2020). The enhanced charge transfer rate usually results in a better catalytic activity of the transducer towards glucose oxidation (Zhou et al., 2019).

3.2. Characterization of ZnO TPs/MXene nanocomposite.
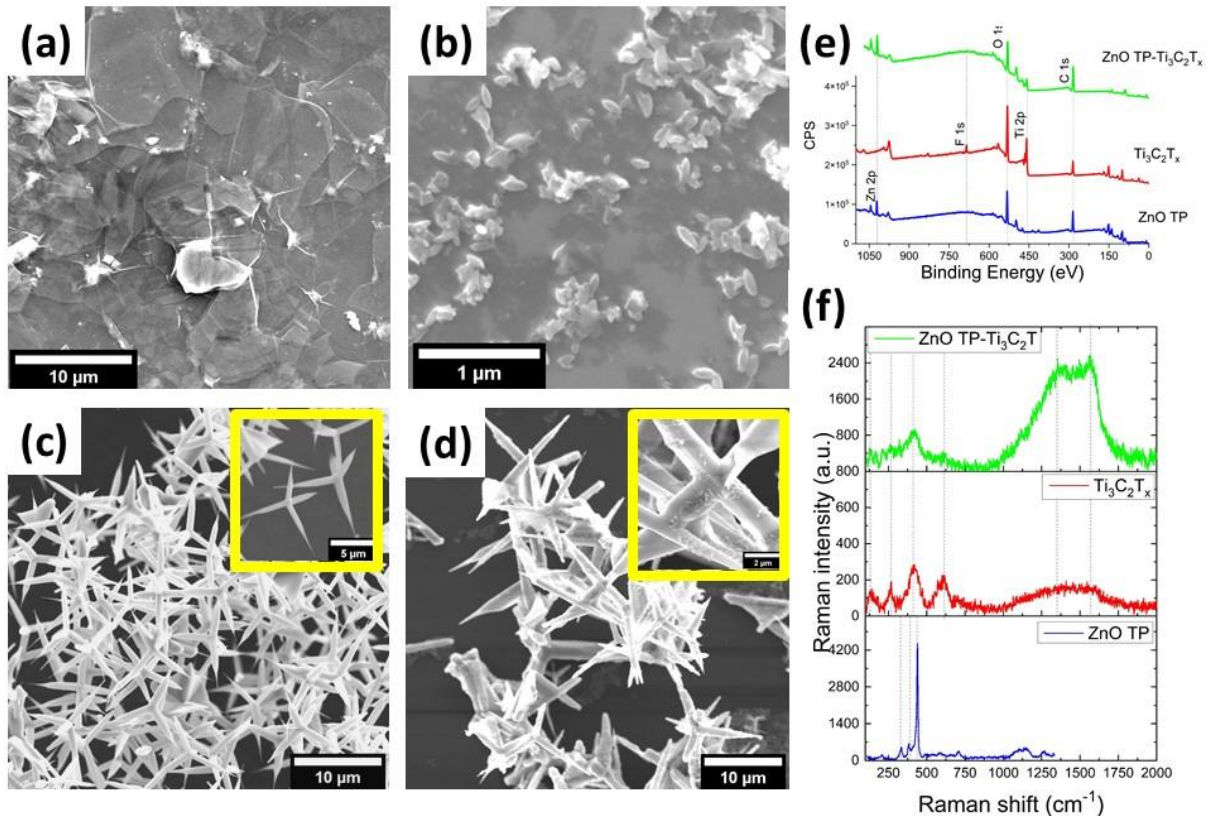
Figure 1. SEM images of **(a)** MXene, **(b)** MXene nanoflakes, **(c)** ZnO TPs and **(d)** ZnO/MXene deposited on the Si substrate; **(e)** survey XPS spectra and **(f)** Raman spectra of produced samples (ZnO TPs, MXene nanoflakes and ZnO/MXene).

MXene $Ti_3C_2T_x$ flakes and then nanoflakes were successfully synthesized from a titanium aluminum carbide (Ti_3AlC_2) MAX phase using a method described in the Experimental section. Fig. 1a, b show SEM images of as-synthesized and nanoflakes of MXene ($Ti_3C_2T_x$), respectively. The lateral size of the delaminated MXene flakes is approximately 7-8 µm, whereas the nanoflakes have a leaf-shaped morphology with an average diameter around 100 nm, indicating the use of a high-power ultrasonic treatment may induce structural changes. Fig. 1c indicates that as-synthesized ZnO TPs are well faceted and consist of four "legs" connected to a central nucleus with an average length of 8 ± 2 µm and a diameter of 400 ± 150 nm (SI, Fig. S3). ZnO TPs have hexagonal morphology, which suggests a single crystalline structure with preferred growth direction along the c-axis of the hexagonal unit cell. The zeta-potential values for ZnO TPs and MXene nanoflakes were 35 ± 8 mV and -27 ± 1, respectively, which provides a strong electrostatic interaction between those two components. Despite this, it was necessary to carry out an additional chemical treatment (APTES treatment, see Experimental section) to obtain a conformal layer of MXene nanoflakes over ZnO TPs (Fig. 1d). Otherwise, an uneven distribution of MXene nanoflakes on the ZnO surface was observed (SI, Fig. S1).

To analyze the chemical composition and electronic states of produced nanocomposites, XPS analysis and Raman spectroscopy were applied. The survey spectra for ZnO TPs, MXene nanoflakes and ZnO/MXene nanocomposites are displayed in Fig. 1e. The spectrum of the ZnO TPs sample displays the signals of Zn, O and C. The XPS analysis of core level Zn 2p spectra (the difference Zn $2p_{3/2}$ - Zn $2p_{1/2}$ = 23.1 eV) indicated the wurzite phase of ZnO (SI, Fig. S4) (Iatsunskyi et al., 2017). Four main elements (oxygen (O), titanium (Ti), carbon (C) and fluorine (F)) were presented in the MXene samples confirming the formation of $Ti_3C_2T_x$ with functional surface groups of –OH and –F. After the formation of ZnO/MXene nanocomposite the peak relating to the F element vanished, indicating the formation of the interface between ZnO and MXene-Ti_3C_2. The detailed XPS analysis of the fabricated ZnO/MXene nanocomposite is provided below and in the supporting information.

Fig. 1f shows the Raman spectra of produced ZnO/MXene nanocomposites and pristine components. As-synthesized ZnO TPs exhibits Raman peaks at 440, 390, and 338 cm^{-1} corresponding to E_2(high), E_1(TO), A_1(TO) modes of ZnO wurzite phase crystal, respectively (Zhang et al., 2009). The Raman spectrum of pristine $Ti_3C_2T_x$ nanoflakes consists of a minimum of five vibrational modes: 125, 255, 425, 608, and 1520 cm^{-1}. Recently, it was shown that a Raman spectrum of $Ti_3C_2T_x$ consists of many peaks in the 100-800 cm^{-1} range, and it can be distinguished into several spectrum regions (Sarycheva and Gogotsi, 2020). According to the Sarycheva *et al.* (Sarycheva and Gogotsi, 2020), one may conclude that the Raman mode at 125 cm^{-1} is attributed to the resonant plasmonic peak. Two Raman modes at 255 and 425 cm^{-1} are associated with out-plane (A_{1g}) and in-plane (E_g) vibrations of C, Ti atoms and surface groups (–OH, –F). The peak at 608 cm^{-1} indicates the carbon vibration (E_g, A_{1g}). The broad Raman peak at 1520 cm^{-1} is attributed to the D and G bands of amorphous and graphitic carbon. Peaks relating to anatase and rutile phases (140, 512 cm^{-1} and 393, 587 cm^{-1}) were not observed, indicating the presence only –OH group on the surface of MXene nanoflakes. As for ZnO/MXene nanocomposites, one can observe the changes of Raman spectrum. Apart from graphitic carbon bands, there are four weak peaks at 133, 170, 213, and 414 cm^{-1}. It is clearly seen that the resonance peak shifted to higher wavenumbers. On the other hand, Raman modes associated with in-plane vibrations of functional groups shifted to the red region. These shifts of both modes and the high-intense D band can be explained by an increased concentration of defects that are formed during the production of ZnO/MXene nanocomposites (Sarycheva and Gogotsi, 2020).
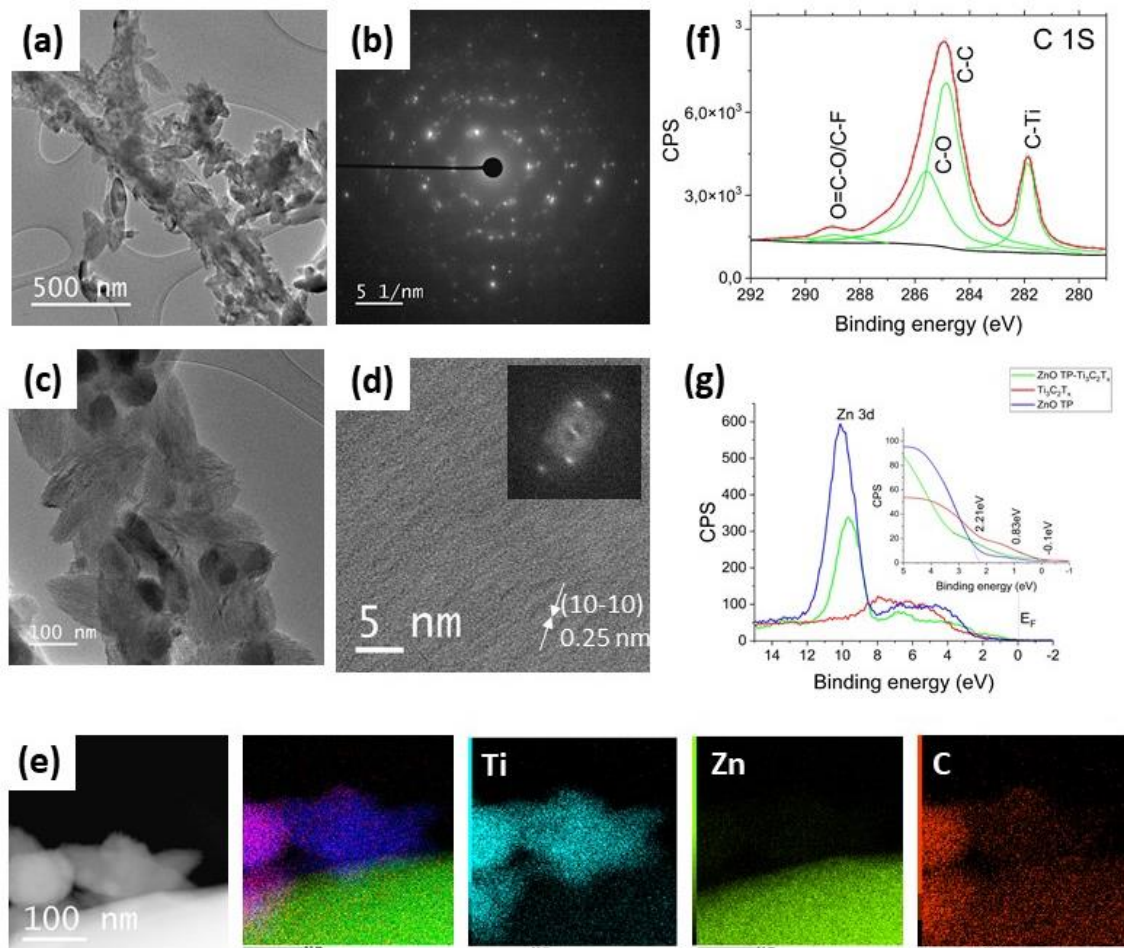
Figure 2. (a-d) TEM and SAED images of ZnO/MXene nanocomposites; **(e)** EDX element map scanning images of the interface between ZnO and MXene nanoflakes; **(f)** the carbon core-level XPS spectrum of ZnO/MXene nanocomposites; **(g)** Valence-band XPS spectra of ZnO TPs, MXene nanoflakes and ZnO/MXene nanocomposites.

The detailed structural and chemical properties of ZnO/MXene nanocomposites were analyzed using TEM and XPS (including Valence Band XPS). Fig. 2a demonstrates the separate "leg" of ZnO TPs covered by MXene $Ti_3C_2T_x$ nanoflakes. The uniform distribution of nanoflakes is clearly seen over the whole surface of ZnO (Fig. 2c, SI, Fig. S5). The corresponding selected area electron diffraction (SAED) pattern demonstrates the polycrystalline nature of ZnO/MXene nanocomposites (Fig. 2b). Fig. 2d shows the high-resolution TEM image of the separate MXene nanoflakes. The lattice parameter of the $Ti_3C_2T_x$ corresponding to $(10\bar{1}0)$ planes is measured to be about 0.255 nm. EDX elemental mapping images for the interface of $ZnO-Ti_3C_2T_x$ are shown in Fig. 2e. The uniform distribution of zinc, titanium, and carbon confirms the formation of the interface between the ZnO surface and $Ti_3C_2T_x$ MXene nanoflakes.

The high-resolution XPS spectra of C 1s and other elements for ZnO/MXene nanocomposites were analyzed (Fig. 2f; SI, Fig. S6). The core level C 1s peak was fitted with four main components at 281.9, 284.8, 285.6, and 289.0 eV, which were attributed to C−Ti, C−C, C−O and C=O−O/C-F, respectively (Näslund et al., 2020). O 1s deconvoluted spectra (SI, Fig. S6) displays three main components at 529.7, 531.5, and 532.9 eV corresponding to O^{2-}, -OH surface groups and absorbed water, respectively (Näslund et al., 2020). Recently, it was shown that Ti−O bonds are the most stable among the terminated groups of $Ti_3C_2T_x$ MXene (Liu and Li, 2018). One may conclude that most terminated groups after the formation of ZnO/MXene nanocomposites are Ti-OH bonds, which was also confirmed by the high-resolution XPS Ti 2p peak (SI, Fig. S6).

One may suggest, both chemical and physical interactions between ZnO surface and MXene may lead to changes in the energy bands of obtained nanocomposites. To study this, the valence band (VB) XPS analysis was used, which can provide valuable information about the modification of the ZnO/MXene electronic structure. Fig. 2g demonstrates the VB spectra for ZnO TP, $Ti_3C_2T_x$ nanoflakes and ZnO/MXene nanocomposites. Typically, the VB spectrum determines the density of states (DOS) below the Fermi level. In the case of ZnO TPs samples, it consists of two components/bands at about 10 eV and 5 eV corresponding to Zn 3d and O 2p orbitals, respectively (Iatsunskyi et al., 2017). The broad VB XPS peak at 8-3 eV for pristine $Ti_3C_2T_x$ MXene may be associated with the C 2s – Ti 3d hybridization region and the terminated groups on the surface (Magnuson et al., 2018). The VB maximum (VBM) for those samples was evaluated using the standard method as previously described (Iatsunskyi et al., 2021). The VBM values were estimated to be 2.2 eV below and 0.1 eV above the Fermi level (E_F) for ZnO TPs and MXene, respectively. A high DOS above E_F is correlated to the low resistivity of $Ti_3C_2T_x$ MXene. After the formation of ZnO/MXene nanocomposite, one may observe the shift to the lower energies of Zn 3d peak, confirming the chemical interaction of MXene nanoflakes with a ZnO surface. In addition, the estimated value of VBM for the ZnO/MXene nanocomposite becomes significantly lower (0.83 eV) in comparison to as-prepared ZnO TPs. It may be suggested the decreasing of the overall resistivity what must provide the enhanced electrocatalytic efficiency. Besides, according to the "d-band center theory", the modification of VBM can optimize the catalytic ability for the produced nanocomposites (Hammer and Nørskov, 2000).

3.3. Electrochemical properties of the fabricated electrodes.
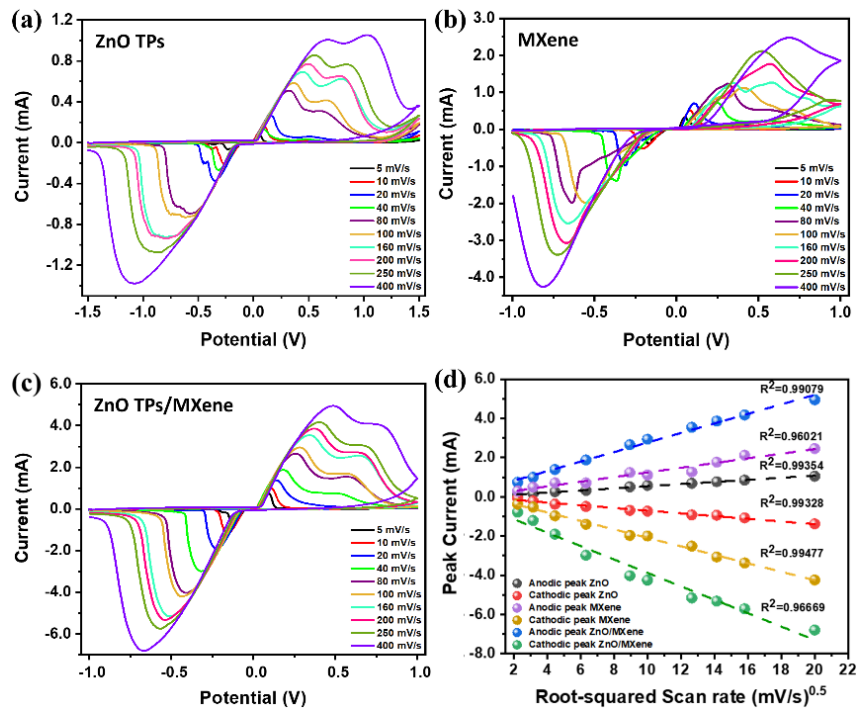
Figure 3. **(a)** CV curves of ZnO TPs/GOx-based electrode, **(b)** MXene/GOx-based electrode, **(c)** ZnO TPs/MXene/GOx electrodes-based electrode scanned in 0.3 mM of glucose in PBS (pH = 7.4) at different scan rates from 5 to 400 mV/s. **(d)** The calibration plots of the anodic and cathodic peak currents *vs* the root-squared scan rate (for ZnO/GOx-, MXene/GOx-, and ZnO/MXene/GOx-based electrodes).

In order to study the electrochemical behavior of prepared skin-attachable electrodes based on ZnO TPs/GOx, MXene/GOx, and ZnO TPs/MXene/GOx, the CV curves were recorded at different scan rates, and obtained plots are shown in Fig. 3. The CV of ZnO TPs/GOx-based electrode (Fig. 3a) indicates that the peak current increases as the scan rate rises, pointing to the quasi-reversible redox reaction (Hu et al., 2011). The quasi-reversibility was also observed for electrodes based on MXene/GOx (Fig. 3b) and ZnO TPs/MXene/GOx (Fig. 3c). Fig. 3d shows that the peak current *vs*. the square root of scan rate is linear (R^2 vary from 0.96021 to 0.99477) for all samples, which indicates a typical diffusion-controlled electrochemical behavior (Tian et al., 2015). In addition, the electron transfer rates between ZnO TPs-, MXene-, and ZnO TPs/MXene-based electrodes and immobilized GOx were calculated according to the Laviron formulation using the following equations (Laviron, 1979):

$$E_{p,c} = E^{o\prime} - \frac{2.3RT}{\alpha nF} \log\left[\frac{\alpha nFv}{RTk_s}\right] (1)$$

$$E_{p,a} = E^{o\prime} - \frac{2.3RT}{(1-\alpha)nF} \log\left[\frac{(1-\alpha)nFv}{RTk_s}\right] (2)$$

where $E_{p,a}$ is the potential of the anodic peak, $E_{p,c}$ is the potential of the cathodic peak, $E^{o\prime}$ is the standard surface potential calculated by averaging the anodic and cathodic potentials at slow scan rates, v is the scan rate, α is the electron-transfer coefficient, k_s is the electron-exchange rate constant, R is the ideal gas constant, T is the absolute temperature *(K)*, F is the Faraday constant, and n is the number of electrons transferred. Electron transfer parameters (α, and k_s) were determined by plotting E_p *vs*. the log of the scan rate (Laviron plots) (Oztekin et al., 2011). Using the slopes of linear portions of the Laviron curves (not shown here) for the ZnO TPs/GOx-, MXene/GOx-, and ZnO TP/MXene/GOx-based electrodes, the electron transfer constants were calculated as 0.46 ± 0.09, 0.67 ± 0.11, and 0.4 ± 0.04, respectively, while the electron-exchange rate constants were determined equal to 0.48 ± 0.03 s^{-1}, 0.36 ± 0.08 s^{-1}, 1.01 ± 0.11 s^{-1}, respectively. The analysis of the obtained k_s values shows that ZnO TP decorating by MXene facilitate the transfer of electrons between the GOx and the electrode. Generally, the higher value of electron-exchange rate indicates the lower resistivity of electrode modifier. The electrochemical impedance spectroscopy (EIS) confirmed the lower resistivity of ZnO TP/MXene in comparison to the pure ZnO TP electrode (SI, Fig. S7).

The above results comply well with the recently reported results for Ti$_3$C$_2$/ZnO composites, where the interaction between ZnO and Ti$_3$C$_2$ (MXene) facilitates the electron transport (Wang et al., 2016). Authors also have shown that the rate capacity, in turn, was directly related to the enhanced surface to volume ratio of Ti$_3$C$_2$/ZnO and an increase in the number of three-dimensional channels for the fast electron transport and the fast ion diffusion (Wang et al., 2016). Moreover, another 2D conductive material, like graphene, was already used to decorate ZnO nanomaterials, which led to a 3-fold increase in catalytic activity due to an increase in the electron transfer rate by 3-4 times as compared to a bare ZnO-based electrode (Xu et al., 2011). Thus, on the basis of the foregoing, it was suggested that an increase (2-3 times) in the electron exchange rate for the ZnO TPs/GOx –based electrode may lead to its better catalytic activity towards glucose oxidation. Additional experiments were also carried out to confirm

### 3.4. CV-based sensor performance.

CV-based measurements were performed to test the catalytic oxidation of glucose on GOx produced electrodes. For this purpose, various glucose concentrations were sequentially added to the electrochemical cell containing PBS with ZnO TPs/GOx-, MXene/GOx-, and ZnO TPs/MXene/GOx-based electrodes (one type of electrode per experiment). CV curves were measured in PBS solution under stirring conditions to achieve a homogeneous glucose distribution in the electrochemical cell. Depending on the electrode, the range of the recorded potential varied from -1 V to 1 V for ZnO TPs/GOx- and ZnO TPs/MXene/GOx-based electrodes (SI, Fig. S8a, b), and -0.6 to 0.6 V for MXene/GOx-based electrodes (SI, Fig. S8c), and the scanning rate was chosen equal to 40 mV/s. Fig. SI, Fig. S8d demonstrates the peak current *vs* the natural logarithm of the glucose concentrations

(sensitivity: 0.54 ± 0.09 mA mM^{-1} cm^{-2}, measured in the CV mode for ZnO TPs/MXene/GOx-based electrode within the physiological range of blood glucose (0 to 20 mM). The sensitivities for ZnO TPs/GOx-, and MXene/GOx-based electrodes were calculated as 0.45 ± 0.06 mA mM^{-1} cm^{-2}, and 0.43 ± 0.07 mA mM^{-1} cm^{-2} indicating the lower glucose sensitivity in comparison to ZnO TPs/MXene/GOx-based electrode. It is seen that the cathodic and anodic currents gradually increase with the glucose concentration, indicating the glucose electrocatalytic oxidation behavior for ZnO TPs/GOx-, MXene/GOx-, and ZnO TPs/MXene/GOx-based electrodes. The typical reactions occurring at the working electrode can be described as following (Kim et al., 2014):

$$\text{glucose} + O_2 + H_2O \leftrightarrow \text{gluconic acid} + H_2O_2, \quad (3)$$
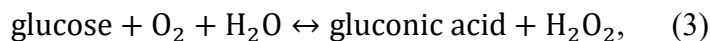
while, the reaction occurring at the counter electrode can be expressed by the following equation (Kim et al., 2014):

$$H_2O_2 \leftrightarrow 2H^+ + O_2 + 2e^- \quad (4)$$
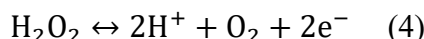
Thus, the detection of glucose can be carried out in both the CV mode and the linear sweep voltammetry (LSV) mode (Tian et al., 2015), measuring signals corresponding to hydrogen peroxide oxidation or dissolved oxygen reduction (free oxygen is consumed during the oxidation of glucose to gluconic acid by GOx in the surroundings of the working electrode). The later approach is based on the decrease of the cathodic current (oxygen reduction reaction – ORR) upon the addition of glucose. The operation in the cathodic regime (negative potentials) allows one to eliminate the effect of interference species. Besides, it is clearly seen the shift of the reduction potential of ZnO TPs/MXene/GOx-based electrode to the lower values (-0.21 V) in comparison to the ZnO TPs/GOx-based electrode. According to this, one may conclude that MXene enhance the catalytic activity of produced nanocomposites.

3.5. Chronoamperometry-based sensor performance in PBS (pH = 7.4).
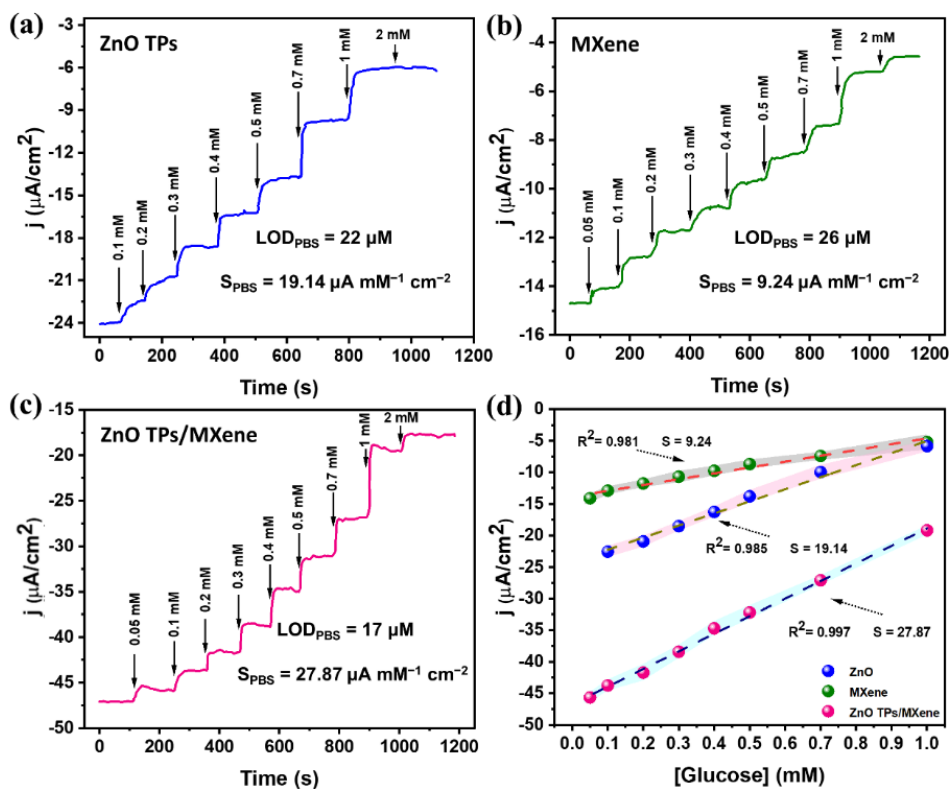
Figure 4. **(a)** Chronoamperometry measurements in PBS with different concentrations of glucose for ZnO TPs/GOx-based electrode at applied potential -0.32 V, **(b)** MXene/GOx-based electrode at applied potential -0.24 V, **(c)** ZnO

11

TPs/MXene/GOx-based electrode at applied potential -0.21 V. **(d)** Calibration curves for the ZnO TPs-, MXene-, and ZnO TPs/MXene/GOx-based electrodes.

After a comprehensive analysis of the structural, optical properties, and the electrochemical behavior of the fabricated ZnO TPs/GOx-, MXene/GOx-, and ZnO TP/MXene/GOx-based electrodes, all the necessary parameters were determined for the subsequent chronoamperometric detection of glucose. Fig. 4a-c represents chronoamperometry curves during the sequential addition of glucose to PBS solution for the ZnO TPs/GOx-, MXene/GOx-, and ZnO TP/MXene/GOx-based electrodes, respectively. One may observe the well-known stairs-like behavior of the current response vs. the concentration of glucose biosensors (Chen et al., 2017; He et al., 2019). Working potentials for glucose detection varied depending on the electrode. Fig. 4d shows the linear calibration curves obtained from the stair-like chronoamperometry curves that show current densities *vs* the glucose concentrations. The sensitivities of the ZnO TPs/GOx-, MXene/GOx-, and ZnO TP/MXene/GOx-based electrodes towards the glucose were determined from the slopes of the calibration curves and were estimated to be 19.14 ± 1.4 µA mM^{-1} cm^{-2}, 9.24 ± 1.2 µA mM^{-1} cm^{-2}, and 27.87 ± 2.8 µA mM^{-1} cm^{-2}, respectively. The LODs were calculated using eq. (5) (Myndrul et al., 2021).

$$LOD = 3.3 \cdot \sqrt{n} \cdot \sigma/b, \qquad (5)$$

where σ is the standard deviations of the negative control at small concentrations, n – number of tests, b is the slope of the curve, depicted in Fig. 4d.

The values of LODs were estimated to be 22 ± 1.3 µM, 26 ± 1.8 µM and 17 ± 1.7 µM for ZnO TPs/GOx-, MXene/GOx-, and ZnO TP/MXene/GOx-based electrodes, respectively. One can assume that the higher sensitivity and the lower LOD of ZnO TP/MXene/GOx-based electrode can be attributed to its enhanced electron transfer rate if compared to ZnO TPs/GOx- and MXene/GOx-based electrodes. Recent references show that the sensitivity of the prepared ZnO TPs/MXene/GOx-based electrode is competitive with the reported sensitivities of skin-attachable or screen-printed glucose electrodes (see Table S1).

The mechanism behind these types of amperometric glucose sensors is based on the change in the concentration of free oxygen surrounding the working electrode. The reduction current depends on the activity of the electrode towards the oxygen reduction reaction since a higher oxygen concentration provides a high reduction current, and contrary. In this particular case, the oxygen concentration is governed by the oxidation of the glucose at the hydroxyl (flavin adenine dinucleotide (FAD)) group of GOx, which occurs with free oxygen consumption (González-Gaitán et al., 2017):

$$\text{glucose} + O_2 \xrightarrow{\text{GOx}} \text{D-glucono-}\delta\text{-lactone} + H_2O_2 \qquad (6)$$
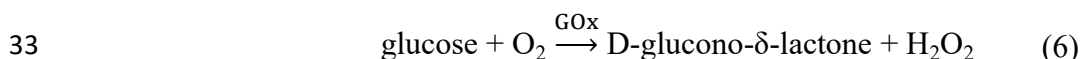
The GOx catalyzes the oxidation of glucose to D-glucono-1.5-lactone with the consumption of O_2 and reduction of FAD to FADH$_2$. Since FADH$_2$ in an aqueous solution tends to be oxidized, it gives the protons to reduce water molecules to H$_2$O$_2$. Depending on the applied potential, either the anodic current for measuring the rate of H$_2$O$_2$ oxidation or the current promoted by the O$_2$ reduction in the cathodic area can be used (Soto et al., 2019).

3.6. Chronoamperometry-based sensor performance in artificial sweat (pH = 6.5).

The sensor was initially intended to be used for qualitative analysis of sweat glucose. Therefore, it was important to test the produced electrode under sweat-like conditions. For this purpose, ZnO TP/MXene/GOx- based electrode was chosen as the most efficient one. All experiments were performed in artificial sweat with pH ~6.5 (detailed information in the experimental section). The amperometric detection showed a similar stairs-like response of current density to glucose concentrations (Fig. 5a). The LDR (in artificial sweat) of the glucose sensor lies between 0.05 and 0.7 mM. The sensitivity to glucose was extracted from the slope of the calibration curve and was about 29.88 ± 2.4 µA mM^{-1} cm^{-2} (Fig. 5b). The value of LOD was calculated to be 21 ± 1.1 µM.
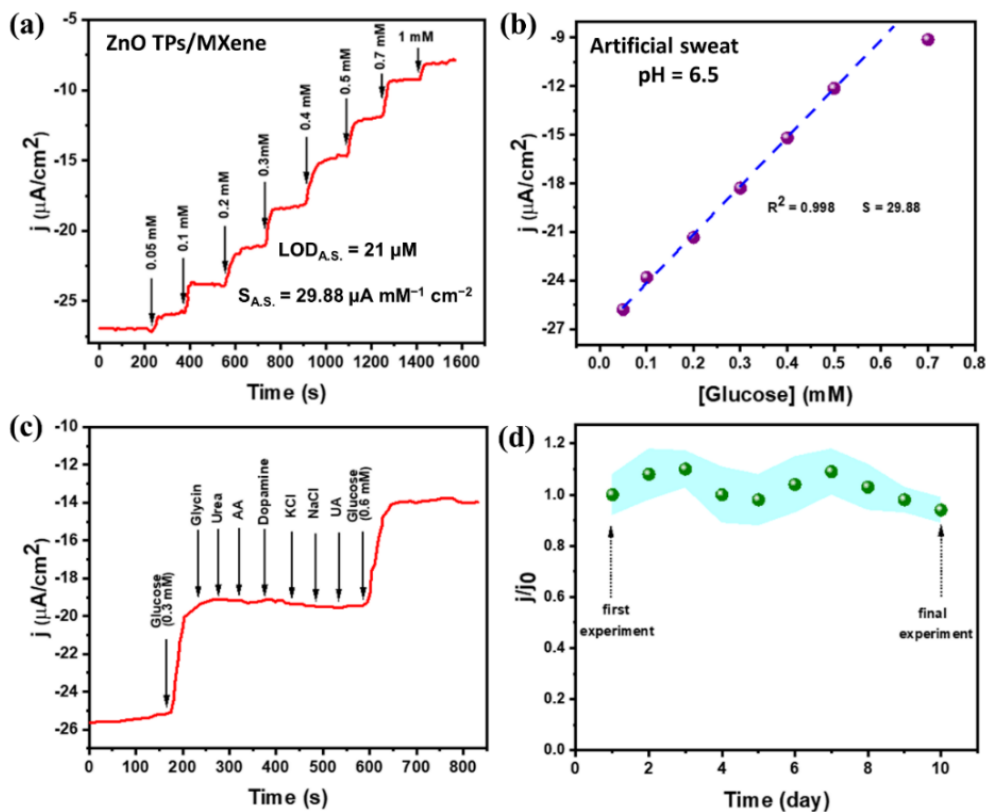
Figure 5. (a) Chronoamperometry measurements for ZnO TPs/MXene/GOx-based electrode in artificial sweat containing different concentrations of glucose (applied potential -0.24 V). **(b)** Calibration curve indicating a linear relationship between the current density of ZnO TPs/MXene/GOx-based electrode and glucose concentration. **(c)** Selective glucose detection by use of ZnO TPs/MXene/GOx-based electrode. **(d)** Long-term stability and multiple use of the ZnO TPs/MXene/GOx-based electrode.

One of the main characteristics of the sensor is its selectivity with respect to various interfering agents contained in the analyte of interest. Fig. 5c shows the selectivity tests of ZnO TPs/MXene/GOx- based electrode to detect 0.3 mM and 0.6 mM of glucose under the interference of different agents such as 0.1 mM AA, 0.5 mM urea, 50 µM UA, 0.05 mM dopamine, 10 mM NaCl, 10 mM KCl, and 0.1 mM glycine. As can be observed, ZnO TPs/MXene/GOx- based electrode provides highly selective glucose detection because of the specific interaction of the glucose and GOx treated ZnO TPs/MXene composites. Moreover, the high selectivity may also be explained by the low applied potential (– 0.24 V) insufficient to oxidize interfering agents (such as AA, UA, etc.) (González-Gaitán et al., 2017).

Fig. 5d represents the long-term stability of the ZnO TPs/MXene/GOx- based electrode for glucose detection during 10 days of the experiments. After each experiment (one per day) the electrode was rinsed in PBS and deionized water, and then stored in a refrigerator at 4°C ready to be reused for further tests. The maximum deviation of the current density was about 10%, which barely affects the sensitivity of the ZnO TPs/MXene/GOx- based electrode up to 10 days. Besides, the reproducibility of produced ZnO TPs/MXene/GOx- based electrodes was studied. Twelwe sets of samples/electrodes were produced using the same protocol. The deviation of sensor performance parameters was about of 10% (SI, Fig. S9).

3.7. Sensors performance under different applied strains.

Considering skin-attachable sensor performance, studying its stability under various mechanical stresses is important. This research analyzed the sensor's performance of ZnO TPs/MXene/GOx-

based electrodes under different applied strains ranging from 0% to 35%. This value of strains range is much enough for flexible sensors to enable its application as a skin-attachable device. Fig. 6a shows the experimental setup for analysis of the stretch abilities of produced sensors. The working, auxiliary, and counter electrodes were sandwiched between slides to prevent the spread out of the analyte and to maintain a constant analyte volume during the experiment. The inset of Fig. 6b shows the relative change of the sensor response, where j and j_0 current densities before and after applied strains, respectively. It can be seen that the ZnO TPs/MXene/GOx electrode demonstrates a stable response (95% – 100%) up to 30% elongation, while significant instability occurs at 35% elongation. It might be explained by the fact that the deformation of ZnO TPs/MXene matrix leads to a decrease in the number of electron path-ways and, consequently, to the current reduction. The glucose detection under application of strains up to 30% (Fig. 6b) showed nearly identical calibration curves (current densities *vs* glucose concentrations) with similar slopes, indicating similar sensitivities and LODs. It may be noted, that the developed ZnO TPs/MXene/GOx-based sensors demonstrate the better or comparable with other stretchable sensors based on CoWO$_4$/CNT (Oh et al., 2018), and v-Au NW-electrodes, where the 30% elongation caused a significant current reduction (~5 times) (Q. Zhai et al., 2019).
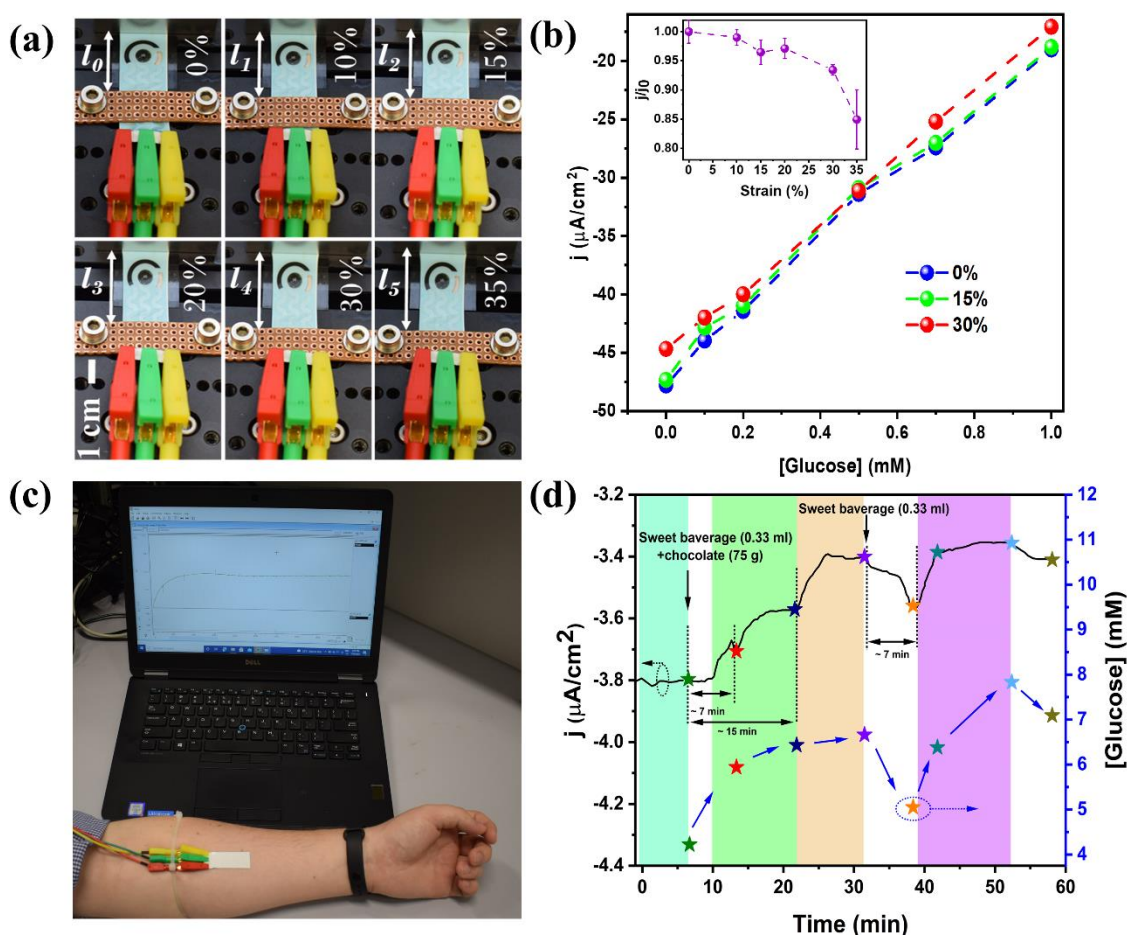
Figure 6. (a) Digital photographs of the stretchable ZnO TPs/MXene/GOx–based electrode at various strains (0% - 35%). **(b)** Performance of the glucose sensor (in artificial sweat) at various applied strains (the insert graph represents the change of ZnO TPs/MXene/GOx electrode current density *vs* applied strains. **(c)** Digital photograph of skin-attachable sensor performance for sweat glucose qualitative analysis. **(d)** Graph representing the current density changes of the ZnO TPs/MXene/GOx-based sensor under the sweets consumption.

3.8. Qualitative glucose monitoring using stretchable ZnO TPs/MXene/GOx electrode.

In the final stage of the research, the developed glucose sensor based on ZnO TPs/MXene/GOx nanocomposites were applied for human sweat analysis. The sensing skin-attachable pathway is depicted in Fig. 6c. The change in current density was recorded in real-time, during sweets consumption and exercising after the signal stabilization (blue area, Fig. 6d). The sweets were followed by exercises (squats) to stimulate sweating, which is associated with higher post-meal blood glucose levels (Lee et al., 2018). It is considered that sugar from beverages is absorbed in the intestine within 10-15 minutes (Wolever, 2003), which corresponds to the decrease in current density and its saturation within 15 minutes (the light green area in Fig. 6d).

Such a behavior of the current density correlates well with the experiments in PBS and artificial sweat, thereby pointing to the increment of the glucose content (post-meal glucose) in a naturally produced sweat. The second decrease in current density (light orange area) may be due to the sugar from the chocolate as it takes longer time (15-30 min) to reach the bloodstream (Shaw et al., 2020). After the two-stage decline (up to 31th min), the current density increased (31-38 min), indicating a drop in the sweat glucose. This decrease in post-meal sweat sugar may be related to muscle glucose uptake during exercise (Sylow et al., 2017). Then, the second dose of sweet beverage was consumed (at 32 min) to increase the glucose level. It is seen that the current density decreased again, thereby confirming the similar behavior of the skin-attachable sensor after the glucose level increased. In parallel with the qualitative glucose monitoring in sweat, the conventional approach for glucose levels detection has been performed by using a commercially available blood glucometer. It is obvious that the sweat glucose real-time monitoring and discrete measurements by means of glucometer had similar trends as shown in Fig. 6d. Moreover, the real-time measurement of the current density of the amperometric glucose sensor correlates well with the other sensors for post-meal glucose monitoring (Bae et al., 2019; Chen et al., 2017; Zaharieva et al., 2019). In addition, qualitative glucose monitoring was performed in a second volunteer, and the results demonstrated the similar trend (SI, Fig. S10).

CONCLUSIONS

In this study, ZnO TPs/MXene-based electrodes were fabricated and used for on-body qualitative glucose monitoring in sweat. The synthesis of ZnO TPs/MXene was performed in accordance with the three-step manufacturing process, including the synthesis of MXene and ZnO, with the following decoration of ZnO TPs with MXene nanoflakes. The fabricated sensors exhibited high sensitivity of 27.87 $\mu A\ mM^{-1}\ cm^{-2}$ and 29.88 $\mu A\ mM^{-1}\ cm^{-2}$ for tests in PBS and artificial sweat, respectively. Moreover, none of the interfering agents affected the sensor response, which indicates the high selectivity of the produced ZnO TPs/MXene/GOx-based electrodes. The long-term stability of the sensor was studied during a 10-days experiment, and the result showed that the sensor response remains stable within this period. The ZnO TPs/MXene/GOx-based electrode demonstrated mechanical stability of up to 30% elongation, with an insignificant change of the detection parameters. The real-time monitoring of post-meal glucose levels in sweat had the same trend as when measured with a conventional blood glucometer under similar conditions. The developed skin-attachable and stretchable electrodes based on ZnO TPs/MXene nanocomposites demonstrate a prospective approach towards non-invasive, continuous glucose monitoring in sweat for healthcare applications.

REFERENCES

Alhabeb, M., Maleski, K., Anasori, B., Lelyukh, P., Clark, L., Sin, S., Gogotsi, Y., 2017. Chem. Mater. 29, 7633–7644. https://doi.org/10.1021/acs.chemmater.7b02847

Bae, C.W., Toi, P.T., Kim, B.Y., Lee, W. Il, Lee, H.B., Hanif, A., Lee, E.H., Lee, N.-E., 2019. ACS Appl. Mater. Interfaces 11, 14567–14575. https://doi.org/10.1021/acsami.9b00848

Chen, Yihao, Lu, S., Zhang, S., Li, Y., Qu, Z., Chen, Ying, Lu, B., Wang, X., Feng, X., 2017. Sci. Adv. 3, 1–8. https://doi.org/10.1126/sciadv.1701629

Cucciniello, M., Petracca, F., Ciani, O., Tarricone, R., 2021. npj Digit. Med. 4, 144. https://doi.org/10.1038/s41746-021-00517-1

Fan, F.R., Wang, R., Zhang, H., Wu, W., 2021. Chem. Soc. Rev. 50, 10983–11031. https://doi.org/10.1039/C9CS00821G

González-Gaitán, C., Ruiz-Rosas, R., Morallón, E., Cazorla-Amorós, D., 2017. RSC Adv. 7, 26867–26878. https://doi.org/10.1039/C7RA02380D

Hammer, B., Nørskov, J.K.B.T.-A. in C., 2000, in: Impact of Surface Science on Catalysis. Academic Press, pp. 71–129. https://doi.org/https://doi.org/10.1016/S0360-0564(02)45013-4

He, W., Wang, C., Wang, H., Jian, M., Lu, W., Liang, X., Zhang, X., Yang, F., Zhang, Y., 2019. Sci. Adv. 5, 1–8. https://doi.org/10.1126/sciadv.aax0649

Hou, C., Yu, H., 2021. Chem. Eng. J. 407, 127192. https://doi.org/10.1016/j.cej.2020.127192

Hu, F., Chen, S., Wang, Chengyan, Yuan, R., Chai, Y., Xiang, Y., Wang, Cun, 2011. J. Mol. Catal. B Enzym. 72, 298–304. https://doi.org/10.1016/j.molcatb.2011.07.005

Iatsunskyi, I., Gottardi, G., Micheli, V., Canteri, R., Coy, E., Bechelany, M., 2021. Appl. Surf. Sci. 542, 148603. https://doi.org/https://doi.org/10.1016/j.apsusc.2020.148603

Iatsunskyi, I., Vasylenko, A., Viter, R., Kempiński, M., Nowaczyk, G., Jurga, S., Bechelany, M., 2017. Appl. Surf. Sci. 411, 494–501. https://doi.org/10.1016/j.apsusc.2017.03.111

Kalambate, P.K., Gadhari, N.S., Li, X., Rao, Z., Navale, S.T., Shen, Y., Patil, V.R., Huang, Y., 2019. TrAC Trends Anal. Chem. 120, 115643. https://doi.org/10.1016/j.trac.2019.115643

Kang, M.-H., Lee, D., Sung, J., Kim, J., Kim, B.H., Park, J., 2019, in: Andrews, D.L., Lipson, R.H., Nann, T.B.T.-C.N. and N. (Second E. (Eds.), Comprehensive Nanoscience and Nanotechnology. Elsevier, Oxford, pp. 55–90. https://doi.org/10.1016/B978-0-12-803581-8.10507-7

Khadidja, M.F., Fan, J., Li, Songyang, Li, Shidong, Cui, K., Wu, J., Zeng, W., Wei, H., Jin, H.-G., Naik, N., Chao, Z., Pan, D., Guo, Z., 2021. Colloids Surfaces A Physicochem. Eng. Asp. 628, 127230. https://doi.org/10.1016/j.colsurfa.2021.127230

Kim, J.Y., Jo, S.Y., Sun, G.J., Katoch, A., Choi, S.W., Kim, S.S., 2014. Sensors Actuators, B Chem. 192, 216–220. https://doi.org/10.1016/j.snb.2013.10.113

Kuranaga, Y., Matsui, H., Ikehata, A., Shimoda, Y., Noiri, M., Ho, Y.-L., Delaunay, J.-J.,

Teramura, Y., Tabata, H., 2020. ACS Appl. Bio Mater. 3, 6331–6342. https://doi.org/10.1021/acsabm.0c00792

Laviron, E., 1979. J. Electroanal. Chem. Interfacial Electrochem. 101, 19–28. https://doi.org/10.1016/S0022-0728(79)80075-3

Lee, H., Hong, Y.J., Baik, S., Hyeon, T., Kim, D., 2018. Adv. Healthc. Mater. 7, 1701150. https://doi.org/10.1002/adhm.201701150

Lee, H., Song, C., Hong, Y.S., Kim, M.S., Cho, H.R., Kang, T., Shin, K., Choi, S.H., Hyeon, T., Kim, D.-H., 2017. Sci. Adv. 3, e1601314. https://doi.org/10.1126/sciadv.1601314

Lei, Y., Luo, N., Yan, X., Zhao, Y., Zhang, G., Zhang, Y., 2012a. Nanoscale 4, 3438. https://doi.org/10.1039/c2nr30334e

Lei, Y., Luo, N., Yan, X., Zhao, Y., Zhang, G., Zhang, Y., 2012b. Nanoscale 4, 3438. https://doi.org/10.1039/c2nr30334e

Liu, R., Li, W., 2018. ACS Omega 3, 2609–2617. https://doi.org/10.1021/acsomega.7b02001

Liu, X., Chen, C., 2020. Mater. Lett. 261, 127127. https://doi.org/10.1016/j.matlet.2019.127127

Lu, P., Wu, J., Shen, X., Gao, X., Shi, Z., Lu, M., Yu, W.W., Zhang, Y., 2020. Adv. Sci. 7, 2001562. https://doi.org/10.1002/advs.202001562

Lv, J., Zhang, L., Zhu, L., Wang, F., Zhang, Y., Zheng, W., Tan, L., 2021. Appl. Surf. Sci. 558, 149863. https://doi.org/https://doi.org/10.1016/j.apsusc.2021.149863

Magnuson, M., Halim, J., Näslund, L.-Å., 2018. J. Electron Spectros. Relat. Phenomena 224, 27–32. https://doi.org/https://doi.org/10.1016/j.elspec.2017.09.006

Meng, L., Turner, A.P.F., Mak, W.C., 2021. ACS Appl. Mater. Interfaces acsami.1c13164. https://doi.org/10.1021/acsami.1c13164

Mishra, Y.K., Adelung, R., 2018a. Mater. Today 21, 631–651. https://doi.org/10.1016/j.mattod.2017.11.003

Mishra, Y.K., Adelung, R., 2018b. Mater. Today 21, 631–651. https://doi.org/10.1016/j.mattod.2017.11.003

Myndrul, V., Coy, E., Bechelany, M., Iatsunskyi, I., 2021. Mater. Sci. Eng. C 118, 111401. https://doi.org/10.1016/j.msec.2020.111401

Myndrul, V., Vysloužilová, L., Klápšt'Ová, A., Coy, E., Jancelewicz, M., Iatsunskyi, I., 2020. Coatings. https://doi.org/10.3390/coatings10121199

Näslund, L.-Å., Persson, P.O.Å., Rosen, J., 2020. J. Phys. Chem. C 124, 27732–27742. https://doi.org/10.1021/acs.jpcc.0c07413

Novoselov, K.S., Geim, A.K., Morozov, S. V., Jiang, D., Zhang, Y., Dubonos, S. V., Grigorieva, I. V., Firsov, A.A., 2004. Science (80-.). 306, 666–669. https://doi.org/10.1126/science.1102896

Oh, S.Y., Hong, S.Y., Jeong, Y.R., Yun, J., Park, H., Jin, S.W., Lee, G., Oh, J.H., Lee, H., Lee, S.-S., Ha, J.S., 2018. ACS Appl. Mater. Interfaces 10, 13729–13740. https://doi.org/10.1021/acsami.8b03342

Oztekin, Y., Ramanaviciene, A., Yazicigil, Z., Solak, A.O., Ramanavicius, A., 2011. Biosens. Bioelectron. 26, 2541–2546. https://doi.org/10.1016/j.bios.2010.11.001

Pavlenko, M., Myndrul, V., Gottardi, G., Coy, E., Jancelewicz, M., Iatsunskyi, I., 2020. Materials (Basel). 13, 1987. https://doi.org/10.3390/ma13081987

Qian, Y., Wei, H., Dong, J., Du, Y., Fang, X., Zheng, W., Sun, Y., Jiang, Z., 2017. Ceram. Int. 43, 10757–10762. https://doi.org/10.1016/j.ceramint.2017.05.082

Sarycheva, A., Gogotsi, Y., 2020. Chem. Mater. 32, 3480–3488. https://doi.org/10.1021/acs.chemmater.0c00359

Sempionatto, J.R., Lin, M., Yin, L., De la paz, E., Pei, K., Sonsa-ard, T., de Loyola Silva, A.N., Khorshed, A.A., Zhang, F., Tostado, N., Xu, S., Wang, J., 2021. Nat. Biomed. Eng. 5, 737–748. https://doi.org/10.1038/s41551-021-00685-1

Shaw, K., Singh, J., Sirant, L., Neary, J.P., Chilibeck, P.D., 2020. Int. J. Sport Nutr. Exerc. Metab. 30, 420–426. https://doi.org/10.1123/ijsnem.2020-0051

Soto, J., Hughes, T., Li, Y.S., 2019. ACS Omega 4, 18312–18316. https://doi.org/10.1021/acsomega.9b02384

Sreedhar, A., Noh, J.-S., 2021. J. Electroanal. Chem. 883, 115044. https://doi.org/10.1016/j.jelechem.2021.115044

Sylow, L., Kleinert, M., Richter, E.A., Jensen, T.E., 2017. Nat. Rev. Endocrinol. 13, 133–148. https://doi.org/10.1038/nrendo.2016.162

Tao, W., Kong, N., Ji, X., Zhang, Y., Sharma, A., Ouyang, J., Qi, B., Wang, J., Xie, N., Kang, C., Zhang, H., Farokhzad, O.C., Kim, J.S., 2019. Chem. Soc. Rev. 48, 2891–2912. https://doi.org/10.1039/C8CS00823J

Tawale, J.S., Dey, K.K., Pasricha, R., Sood, K.N., Srivastava, A.K., 2010. Thin Solid Films 519, 1244–1247. https://doi.org/10.1016/j.tsf.2010.08.077

Tereshchenko, A., Bechelany, M., Viter, R., Khranovskyy, V., Smyntyna, V., Starodub, N., Yakimova, R., 2016. Sensors Actuators B Chem. 229, 664–677. https://doi.org/10.1016/j.snb.2016.01.099

Theerthagiri, J., Salla, S., Senthil, R.A., Nithyadharseni, P., Madankumar, A., Arunachalam, P., Maiyalagan, T., Kim, H.-S., 2019. Nanotechnology 30, 392001. https://doi.org/10.1088/1361-6528/ab268a

Tian, K., Alex, S., Siegel, G., Tiwari, A., 2015. Mater. Sci. Eng. C 46, 548–552. https://doi.org/10.1016/j.msec.2014.10.064

VahidMohammadi, A., Rosen, J., Gogotsi, Y., 2021. Science (80-.). 372. https://doi.org/10.1126/science.abf1581

Wang, F., Cao, M., Qin, Y., Zhu, J., Wang, L., Tang, Y., 2016. RSC Adv. 6, 88934–88942. https://doi.org/10.1039/C6RA15384D

Wang, S., Zhao, J., Tong, T., Cheng, B., Xiao, Y., Lei, S., 2019. ACS Appl. Mater. Interfaces 11, 14932–14943. https://doi.org/10.1021/acsami.9b00267

Wolever, T.M.S., 2003. Nutr. Rev. 61, S40–S48. https://doi.org/10.1301/nr.2003.may.S40-S48

Xu, T., Zhang, L., Cheng, H., Zhu, Y., 2011. Appl. Catal. B Environ. 101, 382–387. https://doi.org/10.1016/j.apcatb.2010.10.007

Yang, Z., Jiang, L., Wang, J., Liu, F., He, J., Liu, A., Lv, S., You, R., Yan, X., Sun, P., Wang, C., Duan, Y., Lu, G., 2021. Sensors Actuators B Chem. 326, 128828. https://doi.org/10.1016/j.snb.2020.128828

Yi, Z., Wang, J., Jiang, T., Tang, Q., Cheng, Y., 2018. R. Soc. Open Sci. 5, 171457. https://doi.org/10.1098/rsos.171457

Zaharieva, D.P., Turksoy, K., McGaugh, S.M., Pooni, R., Vienneau, T., Ly, T., Riddell, M.C., 2019. Diabetes Technol. Ther. 21, 313–321. https://doi.org/10.1089/dia.2018.0364

Zeng, R., Wang, W., Chen, M., Wan, Q., Wang, C., Knopp, D., Tang, D., 2021. Nano Energy 82, 105711. https://doi.org/10.1016/j.nanoen.2020.105711

Zhai, Q., Gong, S., Wang, Y., Lyu, Q., Liu, Y., Ling, Y., Wang, J., Simon, G.P., Cheng, W., 2019. ACS Appl. Mater. Interfaces 11, 9724–9729. https://doi.org/10.1021/acsami.8b19383

Zhai, Y., Zheng, Y., Ma, Z., Cai, Y., Wang, F., Guo, X., Wen, Y., Yang, H., 2019. ACS Sensors 4, 2958–2965. https://doi.org/10.1021/acssensors.9b01436

Zhang, R., Yin, P.-G., Wang, N., Guo, L., 2009. Solid State Sci. 11, 865–869. https://doi.org/https://doi.org/10.1016/j.solidstatesciences.2008.10.016

Zhao, Y., Fu, Y., Wang, P., Xing, L., Xue, X., 2015. Nanoscale 7, 1904–1911. https://doi.org/10.1039/C4NR06461E

Zhao, Y., Yan, X., Kang, Z., Fang, X., Zheng, X., Zhao, L., Du, H., Zhang, Y., 2014. J. Nanoparticle Res. 16, 2398. https://doi.org/10.1007/s11051-014-2398-y

Zhou, F., Jing, W., Xu, Y., Chen, Z., Jiang, Z., Wei, Z., 2019. Sensors Actuators B Chem. 284, 377–385. https://doi.org/10.1016/j.snb.2018.12.141